Contents lists available at ScienceDirect

Materials Today Communications

Method for inverse calculation of erosion parameters in slag-refractory systems

Jerónimo Guarco [a,b,*], Sandra Vollmann [b], Harald Harmuth [b], Burhanuddin [b]

[a] K1-MET GmbH Metallurgical Competence Center, Linz, Austria
[b] Chair of Ceramics, Montanuniversität Leoben, Peter-Tunner Straße 5, 8700 Leoben, Austria

ARTICLE INFO

ABSTRACT

Refractory erosion due to fluid flow is caused by the shear stresses acting on the liquid/solid interface. This mechanism of continuous wear has not been extensively investigated based on appropriate physical considerations. This study proposes a novel method for the inverse calculation of erosion parameters in slag-refractory systems. A computational fluid dynamic model is coupled with optimisation software to solve a nonlinear least-squares problem for the identification of erosion parameters from experimental erosion profiles. Erosion-rate modelling is performed based on a three-parameter law of the acting shear stress. A test problem is studied using artificially generated erosion profiles. The feasibility of the approach with two parameters is proven; however, using three parameters causes the problem to become ill-posed. Moreover, the method is successfully applied to a real experiment with an alumina coarse-grain refractory. Statistical analysis of the solutions is performed for both the test problem and real experimental profile. Confidence intervals and regions calculated via linearisation are examined, but their use is limited and should be evaluated for each case. This method can serve as a basis for further investigations concerning the quantification of refractory erosion.

1. Introduction

Refractory erosion is the mechanism of continuous wear caused by fluid movement along a material surface. The flow is responsible for shear forces that cause detachment of the material grains, which are then washed away in the liquid. Generally, the forces are not sufficiently large to initiate the erosion process; this necessitates preconditioning by corrosion through infiltrated liquid, which weakens the grain/matrix bonds [1,2]. The quantification of refractory erosion has not been extensively investigated based on appropriate physical considerations. One reason for this is the lack of an established erosion law and experimental and computational methods for its depiction.

This study aims to address this problem by introducing a method for the inverse calculation of erosion parameters for refractory materials in liquid slags with experimental erosion profiles. Here, the erosion process is modelled on the macroscale based on Partheniades' equation (Eq. (1)), which is firmly established in the field of soil erosion [3]. The use of this equation is rooted in the similarities between soils and refractories, which are both representable by a grain/matrix structure. The erosion law is a function of the wall shear stress (τ), and the erosion parameters include the critical shear stress (τ_c), which characterises the flow

condition upon which the shear stress is sufficient to begin grain detachment, the rate of detachment k_d [4], and the exponent a.

$$\dot{\varepsilon} = k_d(\tau - \tau_c)^a \tag{1}$$

$\dot{\varepsilon}$ has dimensions of length/time and is considered as a velocity. This is in contrast to most continuous-wear investigations, where the output of the studies is the mass flux density. The units of τ and τ_c are Pa, and the units of k_d depend on the dimensionless power a as follows: $[k_d] = ms^{-1}Pa^{-a}$.

For reference, a study by Hanson and Simon on soil erosion [5] reported τ_c values for cohesive stream beds between 0.001 and 1000 Pa, with values of k_d in the range of 0.001–10 cm^3/(N·s). Their study classified erodibility into five groups, which ranged from very erodible to very resistant. Low values of k_d and high values of τ_c correspond to very resistant soil, whereas large values of k_d and low values of τ_c are indicative of very erodible soil. To measure these parameters, an in-situ jet testing apparatus is prevalently used in soil-erosion investigations [4–7]. The identification of these parameters is typically based on the measurement of scour depth and consideration of equilibrium depth, as described by Hanson and Cook [7]. Exponent a in Eq. (1) is frequently fixed at 1.0 [4,5,7].

Nomenclature

$\dot{\varepsilon}$	erosion rate.
k_d	detachment rate.
τ_c	critical shear stress.
a	exponent.
τ	wall shear stress.
v_θ	swirl velocity.
Ω_1	rotational speed of inner cylinder.
Ω_2	rotational speed of outer cylinder.
μ_Ω	$\frac{\Omega_1}{\Omega_2}$
R_1	radius of the sample.
R_2	radius of the crucible.
d	$R_2 - R_1$ gap width.
η	R_1/R_2 radii ratio.
r	radial coordinate.
Ta	$\frac{2\Omega_1{}^2 d^4\eta^2}{(1-\eta^2)\left(\frac{\mu}{\rho}\right)^2}$ Taylor number.
μ	dynamic viscosity.
ρ	density.
z	axial coordinate.
v_z	axial velocity.
v_r	radial velocity.
Φ	transport scalar.
V	element volume.
∂V	boundary of volume element.
$\overrightarrow{u}$	fluid velocity vector.
$\overrightarrow{u}_g$	mesh velocity vector.
$\overrightarrow{A}$	edge area vector in normal direction.
Γ_Φ	scalar diffusivity.
S_Φ	scalar source term.
Δt	time-step.
n_f	number of faces of a grid element.
δV	volume swept by grid displacement.
w_i	weight function.
X	node coordinates.
X_i	face centroid coordinates.
$\overrightarrow{n}$	unit normal vector.
$\overrightarrow{F}_i$	fictitious force caused by node displacement.
K_{ij}	spring constant.
$\Delta\overrightarrow{x}$	node displacement vector.
θ	$\theta = (k_d, \quad \tau_c, a)^T$.
$\overrightarrow{r}$	residuals vector.
n	number of residual terms.
H	Hessian matrix.
J	Jacobian matrix.
m	number of parameters.
y_i	model response (radial surface coordinate at z_i).
$y_{i,exp}$	experimental value (radial surface coordinate at z_i).
σ	standard deviation.
f_{χ^2}	chi-square probability density function.
Γ	gamma function.
ν	degrees of freedom.
N_{exp}	number of experiments.
s	estimate of standard deviation.
Cov	covariance matrix.
$t_{\nu,0.975}$	critical value of t-student distribution.
Δ^2	95th percentile of χ^2 distribution with m degrees of freedom.
ρ_{k_d,τ_c}	coefficient of correlation between k_d and τ_c.

The jet testing apparatus is not the only approach that can be used to characterise the erosion process of soils. For example, Karmaker et al. [8] conducted an inverse estimation of erodibility parameters using satellite images of eroded river banks at sites with limited accessibility. They applied three different optimisation methods and successfully obtained the erodibility parameters; their study provides an example of how erodibility parameters can be determined from the erosion profile without in situ measurements. Other experimental approaches for soil-erosion investigations include rotating-cylinder experiments and flume tests [9,10].

Although refractory wear via erosion is often quantified in practice by wear measurement, to our knowledge, there is no mathematical treatment in the literature that is similar to that presented herein for refractories. In this study, the coupling of a computational fluid dynamics (CFD) model with an optimisation routine is introduced for the resolution of a nonlinear least-squares problem. This study aims to identify the erosion parameters of Eq. (1) that result in the best fit of the model and the experimental erosion profile.

This study provides a detailed analysis on the feasibility of the proposed method and its applicability to real experimental setups. It is the first presented method for the quantification of refractory erosion with erosion profiles. First, a brief description of the experimental setup is provided in Section 2, followed by a comprehensive description of the simulation model. Subsequently, the implementation of the inverse problem is explained, followed by a description of the test problem, where a statistical assessment of the goodness-of-fit is also discussed. Section 3 is divided between the results of the test problem and those of the real experimental profile. The test problem includes both an exact problem, where the erosion profile is obtained from the simulation, and an artificial problem created by random-noise generation. The inverse calculation is investigated for a model with the three erosion parameters

of Eq. (1) and also with a fixed exponent a of 1.0. Moreover, identification with the inverse calculation was attempted through multiple experiments. Finally, the conclusions are presented in Section 4.

2. Materials and methods

The objective of this study is to establish a method for the inverse calculation of erosion parameters from experimental erosion profiles. This was achieved by coupling CFD simulations with an optimisation solver to solve a nonlinear least-squares problem. The procedure is summarised in the flowchart shown in Fig. 1.

When solving the inverse problem, the model can be considered a black box because no explicit formulas for the relationship between the simulation output and erosion parameters are available. Instead, the
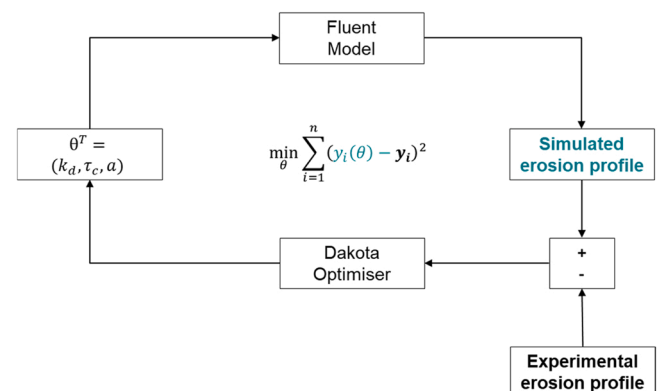

Fig. 1. Coupling of model and optimisation routine.

model is a simulation routine which, in short, consists of solving nonlinear differential equations in a discretised domain through an iterative process. Therefore, this problem must be addressed as a nonlinear one.

The following sections describe the experimental setup, simulation model, and inverse problem.

2.1. Experimental set-up

Kircher et al. presented an experimental setup and method to obtain worn profiles [11]. This provided the experimental basis that is employed in this work for the inverse calculation of erosion parameters using erosion profiles. The experimental setup represented a finger test. These experiments involved a furnace with a temperature that was monitored using thermocouples and maintained at the prescribed value. Inside the furnace, a cylindrical sample of the refractory material was rotated within a slag bath at a constant rotational speed. Fig. 2 shows a schematic description of the experimental set-up, henceforth referred to as a continuous wear-testing device (CWTD). This rotation generated the bath movement and shear forces that act on the refractory surface. After a defined rotation time, the sample was pulled up and left to drip for 30 min. Subsequently, the furnace plug was removed, and a laser device was placed in its position. The laser scanned the surface of the corroded sample while it rotated at 2 rpm. The processing of the laser measurement data and averaging in the circumferential direction provided the necessary erosion profile used for the inverse calculation of the erosion parameters. A detailed description of this setup and the processing of the laser measurements is presented in Ref. [11].

2.2. Simulation model

Simulations of the CWTD experiments were conducted with a CFD model developed using ANSYS Fluent v.19.0; the flow field of the slag bath was resolved, and the refractory merely represented the boundary of the model. The model was a two-dimensional (2D), isothermal, axisymmetric model with swirl. Turbulence was not considered in the model; therefore, the exact Navier–Stokes equations were solved. The assumption of laminar flow was based on a comparison with a bench-

mark problem of fluid dynamics, that is, the flow inside an annular region with rotating cylinders. The first stable flow in such set-ups is a circular Couette (CC) flow, and the azimuthal velocity (v_θ) is given as follows:

$$v_\theta = \Omega_1 \left(\frac{\mu_\Omega - \eta^2}{1 - \eta^2} \right) r + \Omega_1 R_1^2 \left(\frac{1 - \mu_\Omega}{1 - \eta^2} \right) \frac{1}{r}. \tag{2}$$

Centrifugal instabilities appear with increasing rotational speed and the flow-field deviates from the CC flow. Taylor was the first to apply linear stability theory to determine the locus of the first transition [12]. This regime is known as the Taylor vortex flow, where laminar, axisymmetric vortical structures appear. Generally, the transition between different flow structures is determined by the Taylor number (Ta), which represents the ratio between centrifugal and viscous forces [13–16]. For finger-test experiments, the values of the Taylor number are sufficiently low, such that the CC flow is the preferred mode of stability; therefore, a laminar axisymmetric flow is appropriate for the model. Our setup has some fundamental differences to this benchmark problem, such as a relatively short cylinder length, a bottom clearance to the crucible, and a two-phase interface; therefore, this comparison is only done for flow-regimen characterisation. Nevertheless, as will be shown in Section 3, the CC solution provided a good prediction of the velocities in our experiments.

Fig. 3 shows a schematic of the model with the discretised domain and boundary conditions. These include a no-shear condition at the slag/atmosphere interface, a no-slip condition at the crucible wall, a constant rotational speed at the refractory wall, and symmetry around the axis of the rotating sample. Furthermore, the refractory wall is a moving boundary because it is subject to erosion. The continuity equation (Eq. (3)) and governing equations for the axial (v_z), radial (v_r), and azimuthal (v_θ) velocities are given as follows:

$$\frac{\partial}{\partial z}(\rho v_z) + \frac{\partial}{\partial r}(\rho v_r) + \frac{\rho v_r}{r} = 0, \tag{3}$$

$$\frac{\partial}{\partial t}(\rho v_z) + \frac{1}{r}\frac{\partial}{\partial z}(r\rho v_z v_z) + \frac{1}{r}\frac{\partial}{\partial r}(r\rho v_z v_r) = -\frac{\partial p}{\partial z} + \frac{1}{r}\frac{\partial}{\partial z}\left[r\mu\left(2\frac{\partial v_z}{\partial z} - \frac{2}{3}\nabla\cdot\vec{v}\right)\right] + \frac{1}{r}\frac{\partial}{\partial r}\left[r\mu\left(\frac{\partial v_z}{\partial r} + \frac{\partial v_r}{\partial z}\right)\right], \tag{4}$$
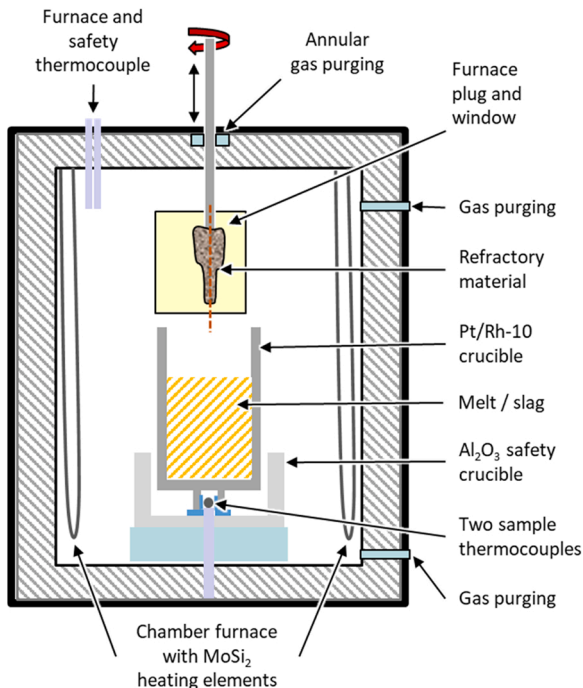

Fig. 2. Schematic of the CWTD.

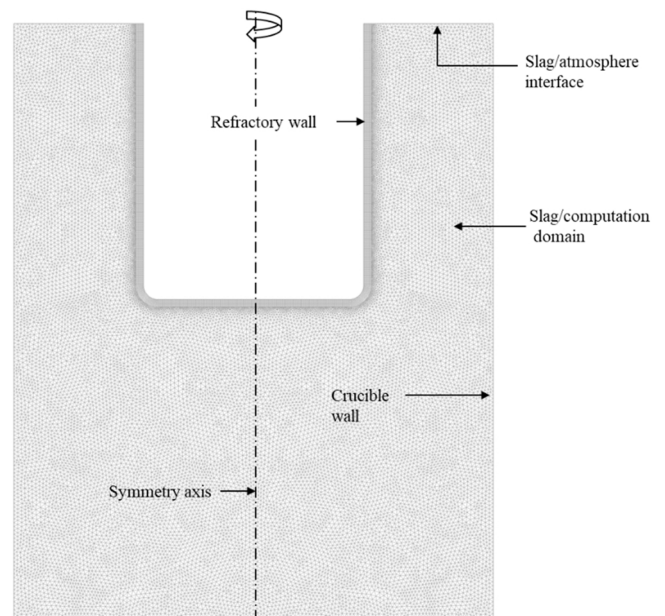**Fig. 3.** Computational domain.

$$\frac{\partial}{\partial t}(\rho v_r) + \frac{1}{r}\frac{\partial}{\partial z}(r\rho v_r v_z) + \frac{1}{r}\frac{\partial}{\partial r}(r\rho v_r v_r) = -\frac{\partial p}{\partial r} + \frac{1}{r}\frac{\partial}{\partial z}\left[r\mu\left(\frac{\partial v_r}{\partial z} + \frac{\partial v_z}{\partial r}\right)\right]$$
$$+ \frac{1}{r}\frac{\partial}{\partial r}\left[r\mu\left(2\frac{\partial v_r}{\partial r} - \frac{2}{3}\nabla\cdot\vec{v}\right)\right]$$
$$- 2\mu\frac{v_r}{r^2} + \frac{2}{3}\frac{\mu}{r}(\nabla\cdot\vec{v}) + \rho\frac{v_\theta^2}{r}, \quad (5)$$

$$\frac{\partial}{\partial t}(\rho v_\theta) + \frac{1}{r}\frac{\partial}{\partial z}(r\rho v_z v_\theta) + \frac{1}{r}\frac{\partial}{\partial r}(r\rho v_r v_\theta) = \frac{1}{r}\frac{\partial}{\partial z}\left[r\mu\left(\frac{\partial v_\theta}{\partial z}\right)\right] + \frac{1}{r^2}\frac{\partial}{\partial r}\left[r^3\mu\frac{\partial}{\partial r}\left(\frac{v_\theta}{r}\right)\right] - \rho\frac{v_r v_\theta}{r}, \quad (6)$$

where $\nabla\cdot\vec{v}$ is

$$\nabla\cdot\vec{v} = \frac{\partial v_z}{\partial z} + \frac{\partial v_r}{\partial r} + \frac{v_r}{r}. \quad (7)$$

The movement of the refractory wall creates a moving boundary problem, in which the slag domain increases with time. This phenomenon was incorporated into the model using dynamic meshing methods. These meshing methods ensure the mesh quality during the simulations necessary for an accurate solution of the governing equations. A description of the dynamic meshing methods and other simulations details can be found in Appendix A in the supplementary material.

2.3. Inverse problem

The model was used with the optimisation software Dakota v.6.11 for the inverse calculation of the erosion parameters $\theta = (k_d, \tau_c, a)^T$. A least-squares problem (Eq. (8)) was formulated with the residual vector $(\vec{r})$ computed from the difference between the experimental and simulated erosion profiles.

$$\min_\theta \quad f(\theta) = \min_\theta \frac{1}{2}\sum_j^n r_j^2(\theta) \quad (8)$$

The resolution of the minimisation problem given by Eq. (8) translates into solving the system of equations for the first-order optimality condition:

$$\frac{\partial f(\theta)}{\partial \theta_i} = 0, \quad i = 1..m. \quad (9)$$

Here, m takes the value of 2 if a is set to unity, and 3 otherwise. The NL2SOL method proposed by Dennis et al. was used as the solver [17]. This is a modified version of the Gauss–Newton (GN) method shown in Eq. (10), where J is the Jacobian matrix, and $\Delta\theta = \theta_{k+1} - \theta_k$ is the difference between the current and next iterations. In the GN method, the Hessian matrix of $f(\theta): H = J_k^T J_k + \sum_{j=1}^n r_j(\theta_k)H(r_{j(\theta_k)})$ is approximated by $J_k^T J_k$, where $H(r_{j(\theta_k)})$ represents the Hessian matrix of the residual term r_j with respect to parameter θ. The method proposed by Dennis et al. [17] consists of an augmentation of this Hessian to include the effects of the terms neglected in the GN method. Furthermore, the method utilises a trust-region method to determine the optimal step length, and it can choose whether augmentation to the Hessian is necessary because in some cases, the GN method will exhibit better performance. The Jacobian was computed using finite differences with a step size of 0.001 relative to each parameter. For convergence, the relative objective function reduction of a full Newton step (no damping of the step through the trust-region method) was compared with the convergence criterion $\varepsilon = 10^{-3}$. This reduction was relative to the minimal actual value of the objective function between the current and previous iteration results.

$$J_k^T J_k \Delta\theta = -J_k^T \vec{r}_k \quad (10)$$

It is necessary for the model to run automatically with the parameters passed by the optimisation solver and return the residuals at the end of the simulation, which is achieved with C-shell scripting. This is performed in conjunction with a Fluent journal file to automate the execution of the CFD model. The first step is the generation of the user defined functions (UDFs) source files with the current erosion parameters. Then, the CFD model is launched with the journal file, the UDFs are compiled, and the simulation is started from a converged steady-state solution and advanced with the prescribed time step for the corresponding erosion time. At the end of the simulation, the erosion profile is printed to a file, namely a profile of the radius of the sample along the axial direction. Because the resolution of the model is not necessarily equal to that of the experimental erosion profile, interpolation of the former into the latter was performed using a Python script based on the NumPy library to calculate the residuals. Each model run used a separate directory, in which the end simulation results were also stored. CFD simulations were conducted without a graphical output and in parallel mode with up to four nodes to reduce the simulation time. The processors were Intel® Core™ i7–3930 K. One iteration of the NL2SOL solver requires one full CFD model run. Additionally, the gradients were computed numerically via forward differences; therefore, each iteration requires $m+1$ simulations for computation, where m is the number of parameters being determined. Depending on the experiment, the computation time needed might be of up to three days for 15 random starting points. Moreover, model failure, that is, the premature ending of the simulation is communicated to the optimisation software in a special way by passing very large residuals to discourage exploration of the solver in this region of the parameter space. Model failure is generally associated with poor meshing issues, which is related to a combination of erosion parameters that results in an excessively high erosion rate.

2.4. Test-problem

A test problem was employed to study the behaviour of the identification method and determine the best choice of solver. The test problem consisted of arbitrarily choosing erosion parameters and constructing artificial experimental data using model prediction and adding artificial noise. Noise was obtained by drawing random numbers from a normal distribution with a zero mean and a given standard deviation. MATLAB's *normrnd* command was used with a standard deviation $\sigma = 10^{-3}mm$. Notably, when the experimental errors are independent and normally distributed, the least-squares solution is also the maximum likelihood solution. This justifies the chosen design of the artificial experiments, particularly because experimental errors are typically normally distributed as a consequence of the central limit theorem [18].

In the test problem, the real solution was known beforehand; thus, the assessment of the solution was straightforward. However, this information was not used to solve this problem. Multiple random initial points were employed to sort out convergence to local minima. If different solutions were encountered, they were discriminated based on the minimal value of the objective function.

Furthermore, the standard deviation of the constructed experimental data was known; therefore, a chi-square (χ^2) test was used to assess the goodness-of-fit provided by the solution. The observed χ_{obs}^2 provides a measurement of the misfit between the experimental data and model,

as defined in Eq. (11). Under the hypothesis used in the least-squares problem, that is, an uncorrelated, normally distributed error with standard deviation σ, this variable is chi-square distributed with $\nu = n - m$ degrees of freedom [18]. For a large ν, at a level of significance $\alpha = 0.05$, χ^2_{obs} must lie in the interval given by Eq. (12) if the model parameter θ represents the experiment. This was used to check the statistical acceptability of the solutions.

$$\chi^2_{obs} = \sum_{i=1}^{n} \frac{\left(y_i(\theta) - y_{i,exp}\right)^2}{\sigma^2} \tag{11}$$

$$\frac{\left(\sqrt{2\nu - 1} - 1.96\right)^2}{2} \leq \chi^2_{obs} \leq \frac{\left(\sqrt{2\nu - 1} + 1.96\right)^2}{2} \tag{12}$$

Moreover, a plot of the residuals scaled by the standard deviation exhibits no clear tendencies, and they appear to be randomly distributed around zero.

In Eq. (11), $y_{i,exp}$ are the values obtained from the superposition of the noise with the simulated radii, and σ is the standard deviation of the noise. With this approach, the behaviour of the problem with different configurations was studied: both a two-parameter erosion rate, obtained by fixing parameter a to 1, ($m = 2$) and a three-parameter rate ($m = 3$) were considered for the noisy generated profiles. Furthermore, an analysis of the exact problem, that is, no noise added to the data, was also conducted, where the chi-square test was not applied because the data had no errors.

For the test problem, a refractory with a radius of 10 mm and an immersion length of 57 mm was considered. The clearance to the crucible bottom was 20 mm, and the crucible radius was 32.5 mm. The slag viscosity and density were 0.6186 Pa·s and 2589 kg/m3, respectively. The Taylor number was 412, which was well below the critical Taylor number of 5231 calculated from DiPrima et al. [13]. Additionally, the Reynolds number with the gap width as the characteristic length is 19.7. Fig. 4 shows the simulated flow field for this setup. Here, a typical CC flow was observed in the annular region, where the velocity magnitude decreased from the prescribed rotational speed at the inner cylinder to zero at the crucible wall.

Fig. 5(a) shows a comparison of the analytical CC solution (Eq. (2)) with our simulation results at two different axial positions: at half the cylinder length and near the sample tip. It is evident that the velocity magnitude is well predicted by the CC solution at the half-length line, with an average relative error of 0.2%, whereas the flow field deviates from the prediction toward the end of the sample. The velocity gradient

at the refractory wall results in the WSS distribution shown Fig. 5(b); the axial coordinate begins at the slag/atmosphere interface and increases toward the tip of the sample. The WSS is the variable of interest that dominates the erosion process, according to Eq. (1). Additionally, in this figure, the theoretical CC-WSS was computed from the analytical solution given in Eq. (13). The simulated WSS deviated from the analytical values more noticeably near the slag/atmosphere interface, where the no-shear boundary condition was imposed, and close to the sample tip, where these stresses were larger.

$$\tau = 2\mu\Omega_l \left(\frac{1 - \mu_\Omega}{1 - \eta^2}\right) \tag{13}$$

3. Results and discussion

3.1. Results of test-problem

The inverse problem was conducted with the following choice of erosion parameters: $\theta = (k_d, \quad \tau_c, a)^T = \left(2 \cdot 10^{-9} m \quad \text{Pa}^{-1} \quad \text{s}^{-1}, \quad 5 \quad Pa, 1\right)$, and the erosion time was 30 min

Simulation with the chosen parameters for 30 min of flowtime permits the computation of our erosion profile, which is shown in Fig. 6. The continuous line represents the model profile used in the exact problem, and the scatter plot represents the solution with random noise added to the data. A grid independence test was conducted, where refining the mesh from 20,307 to 81,228 elements only led to a change of 1.3% on average in the WSS distribution; therefore, the coarser mesh was chosen. Furthermore, a time step of 1 s was used for the simulation, and the independence of this choice was checked by performing simulations with a time step of 0.1 s. The predicted erosion profile changed by 0.001% when the average radius of the sample was considered. Moreover, simulations comparing the multiphase model were conducted, where the surface-tension effects were considered as described in our previous study [19]. However, this approach requires significantly smaller time steps for the stability of the Volume of Fluid solver. Additionally, the results of the single-phase model, where the slag/atmosphere interface is modelled as a no-shear boundary, are in good qualitative agreement with those of the multiphase simulation.

3.1.1. Exact problem, m = 2

The first configuration that was studied was the simplest, where a two-parameter erosion rate was considered by fixing the exponent a to 1, and no artificial noise was added to the simulated profile. The solution of five multiple random starts is summarised in Table 1, where f represents half of the sum of squares of residuals. For the exact problem at the optimum (θ^*), $f(\theta^*)$ is 0.

In all cases, the solution was the true solution with very small values of the objective function, and changes in these values did not affect the parameters, at least in the first five decimals. In most cases, convergence occurs owing to the absolute convergence criterion. Additionally, the determinant of the approximated Hessian matrix is shown in this table; the determinant is similar for all solutions and is indicative of non-singular matrices. Furthermore, the appropriateness of the NLS2SOL solver was verified, which is an ideal outcome, owing to the quadratic convergence of this gradient-based solver.

3.1.2. Exact problem, m = 3

Here, a three-parameter problem and an exact simulated profile were employed. The results for the inverse problem are presented in Table 2.

The first three solutions corresponded to the exact solution, whereas solutions 4 and 5 were different and corresponded to local subminima based on the larger value of the objective function. This highlights the necessity of using multiple random initial points for the inverse calculation. Notably, the determinant of the approximated Hessian matrices were close to zero, and the matrices were close to singular. Aster et al. [18] claimed that in practical cases, this is indicative of an ill-posed
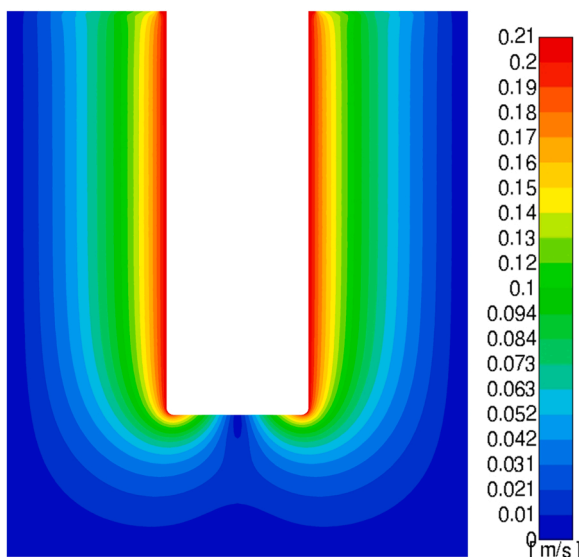

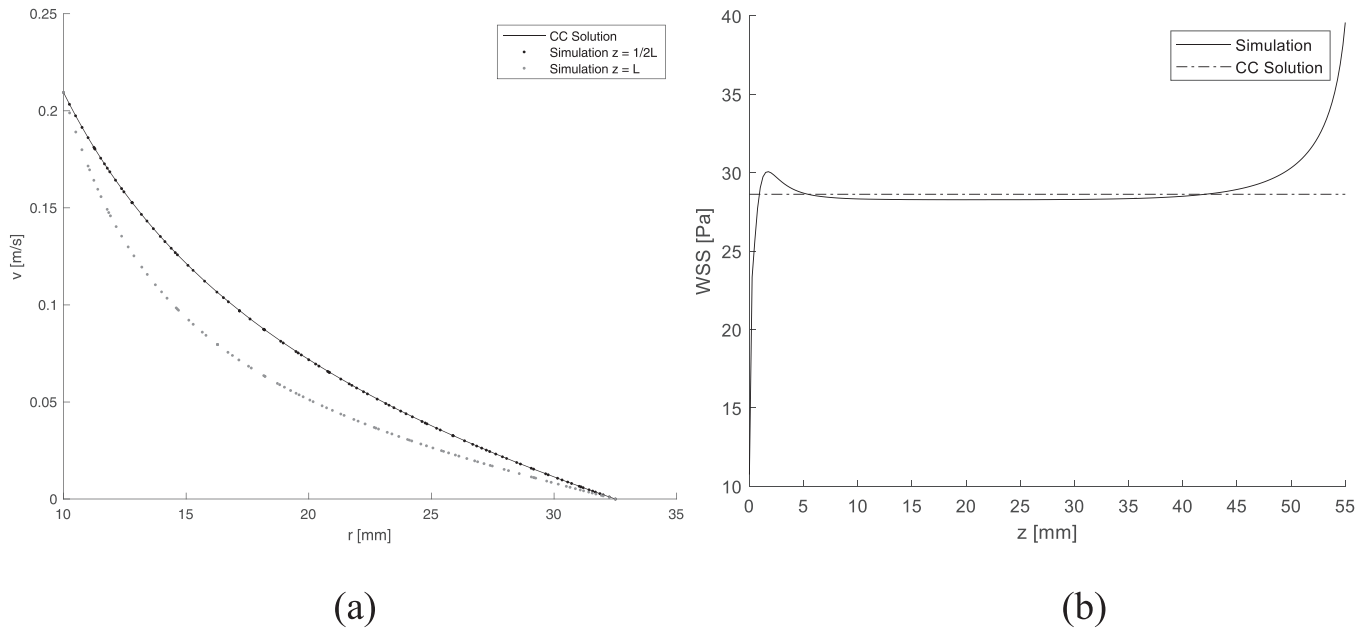**Fig. 4.** Velocity contours of the simulated test-problem.

Fig. 5. Velocity magnitude at different axial positions in the annular gap (a). Wall shear stress profile (b).
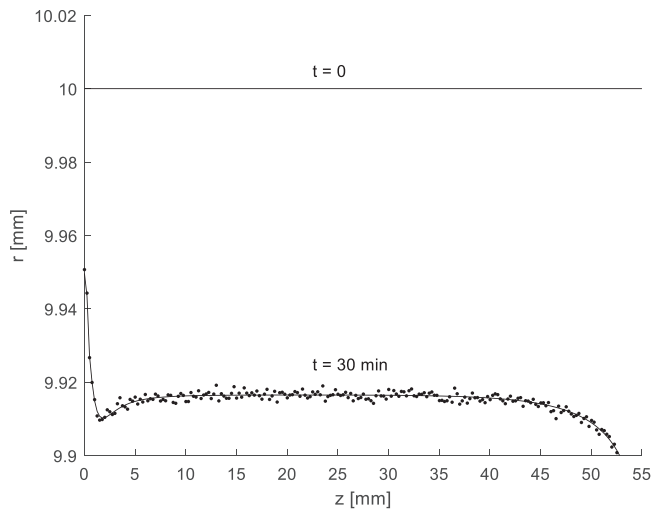

Fig. 6. Erosion profile (exact) and noisy data.

Table 1
Solutions of exact problem with $m = 2$.

	f	k_d (m/s)	τ_c (Pa)	$det(J^T J)$
1	4.00E-22	2.00E-9	5.00	6.55
2	4.50E-22	2.00E-9	5.00	6.56
3	4.50E-22	2.00E-9	5.00	6.56
4	5.00E-22	2.00E-9	5.00	6.59
5	8.35E-22	2.00E-9	5.00	6.54

Table 2
Solutions of exact problem with $m = 3$.

	f	k_d $(m/(s\ Pa^a))$	τ_c (Pa)	a	$det(J^T J)$
1	1.80E-21	2.00E-9	5.00	1.00	4.76E-10
2	5.75E-21	2.00E-9	5.00	1.00	5.09E-10
3	6.60E-21	2.00E-9	5.00	1.00	5.05E-10
4	5.78E-13	9.00E-10	0.005	1.18	9.24E-05
5	5.79E-13	9.00E-10	0.000	1.18	8.81E-05

problem. In this case, the true solution was found; however, the situation with noisy data will be proven to be different.

3.1.3. Artificial experimental problem, m = 2

For these experiments, random noise was added to the simulated profile, as explained in Section 2.4, and the erosion parameters were calculated with a fixed to 1.0. With a known standard deviation σ of random noise, the least-squares problem was transformed such that the residuals were scaled by the standard deviation, as follows:

$$r = \frac{y_i - y_{exp,i}}{\sigma}. \tag{14}$$

The value of the objective function f now represents half of the sum of the squared scaled residuals, and $\chi^2_{obs} = 2f$. The solutions are listed in Table 3.

All solutions with the five random starting points were the same and were close to the parameters used for the design of the problem with errors of 0.2 % and 2 % for k_d and.

τ_c, respectively. The calculated interval for χ^2_{obs} using Eq. (12) was [177.6 259.2], and the reported values lie within this interval. In all cases, the determinant of the Hessian matrix was similar to those presented in Table 1. This was expected because these values are only dependent on the model itself, and the experimental data has no influence on them. Moreover, this matrix was nonsingular, and unique solutions were obtained. In the Fig. 7, the scaled residuals are shown, and they appear randomly distributed with no apparent trends in their distribution.

3.1.4. Artificial experimental problem, m = 3

The same problem was attempted with the power law of the excess shear stress; the results are shown in Table 4 for five different starting

Table 3
Solutions with artificial erosion profile with $m = 2$.

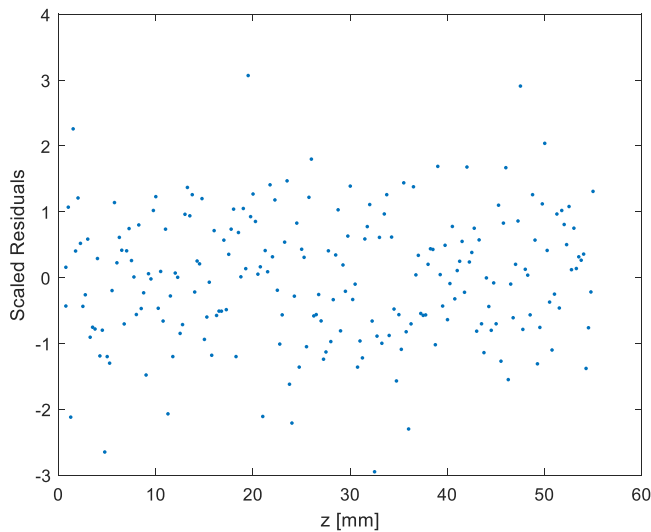|	f	k_d (m/s)	τ_c (Pa)	χ^2_{obs}	$det(J^T J)$
1	101.4	2.0046E-9	5.10	202.7	6.5
2	101.4	2.0049E-9	5.10	202.7	6.6
3	101.4	2.0046E-9	5.10	202.7	6.6
4	101.4	2.0051E-9	5.10	202.7	6.6
5	101.4	2.0046E-9	5.10	202.7	6.5

Fig. 7. Scaled residuals of the solution along the axial coordinate.

points.

In this case, no unique solution was obtained; similar values of the objective function led to different solutions, and none corresponded to the parameters used in the design of the test problem. Moreover, from a statistical point of view, all solutions except solution 5 are acceptable because the values of χ^2_{obs} lie within the calculated interval of [176.7, 258.1]. These solutions all produced the same characteristic erosion rate, which was calculated using the solution parameters and analytical CC-WSS. This is characteristic of an ill-posed problem. This was also noticeable in the determinants of the Hessian matrices, which were indicative of nearly singular matrices. A possible explanation for this behaviour is the relatively low variation in the WSS distribution along the axial coordinate resulting from the CC flow field. This is easily understood when a constant WSS distribution is considered. Then, an infinite combination of parameters would produce the same erosion rate, and therefore, the same erosion profile. Solution number 5 is a case of divergence owing to the repetitive failure of the model, where large residuals are passed.

3.1.5. Artificial experimental problem, $m = 3$, $N_{exp} = 2$

Finally, it is feasible to perform multiple experiments with different erosion times. Here, the determination was attempted using combined data from two experiments: one with an erosion time of 30 min and the other of 15 min, as shown in Table 5.

Convergence to the design optimum was not achieved, and the

multimodality of the problem was evident and explained by the Hessian matrix determinant. Repetition of the experiment, that is, using the same erosion time with a new set of random errors, also led to the same conclusions, shown in Table 6.

3.2. Result from real experiments

The experimental setup consisted of an alumina coarse-grained refractory material. The slag was in the CaO-Al2O3-SiO2-MgO system with weight percentages of 32.42%, 11.16%, 49.56%, and 6.86% for calcia, alumina, silica, and magnesia, respectively. The experimental temperature was 1450 °C, for which the slag density of 2595.2 kg/m3 was calculated from the work of Xin [20]. The slag viscosity was 1.0187 Pas and was calculated with the software FactSage v.7.3. The rotational speed was 200 rpm with an erosion time of 30 min. All the other experimental parameters were as defined in Section 2.4. The results for the five initial random points are presented in Table 7. The information from the test problem already indicated the infeasibility of inverse calculation with $m = 3$; therefore, we attempted the determination with a at a fixed value of 1.

The results are unique and differed only in decimals, owing to the premature convergence of the solver. The solution is shown graphically in Fig. 8 with the worn profile measured by the laser device as described in Section 2.1 and the simulation curve with the optimal parameters. In this figure the fit between the model and experiment can be estimated. The largest discrepancies between the model and experimental data were observed in the slag/atmosphere near z below approximately 5 mm. This may have been caused by parameters k_d and τ_c not being constant over the entire specimen length. Lower erodibility was expected close to the slag surface because this region might be less affected by pre-corrosion. This effect could be cancelled by evaluating the profile for $z > 5$ mm only. Notably, the determinants of the Hessian matrices were indicative of a nonsingular matrix (see Table 7).

The standard deviation was not known when the real experimental erosion profiles were used. One approach is to approximate the standard deviation from the residuals, as per Eq. (15). This incurs a statistical cost, and with this standard deviation, the solution always passes the chi-square test; therefore, other methods for statistical assessment are necessary.

$$s = \sqrt{\frac{\sum_i^n (y_i(\theta) - y_{i,exp})^2}{\nu}} \tag{15}$$

Confidence intervals and regions were calculated to evaluate the solutions. Here, a nonlinear problem was considered, but the calculations for confidence intervals and regions were based on the linearisation of the model, as described in the literature [18,21]. This

Table 4
Solutions with artificial erosion profile and $m = 3$.

	f	k_d $(m/(s\,Pa^a))$	τ_c (Pa)	a	χ^2_{obs}	$\dot{\varepsilon}_{CC}$(m/s)	$det(J^T J)$
1	101.4	2.77E-9	7.16	0.92	202.7	4.715E-8	3.48E-10
2	101.7	1.30E-9	2.39	1.10	203.5	4.715E-8	1.49E-09
3	101.9	1.16E-9	1.65	1.13	203.8	4.715E-8	2.02E-09
4	102.0	4.07E-9	9.65	0.83	204.1	4.715E-8	3.18E-10
5	1E14	6.07E-9	8.73	1.43	2E14	4.310E-7	-

Table 5
Solutions with artificial erosion profile for $m = 3$ using two experiments (t = 15 min and t = 30 min erosion).

	f	k_d $(m/(s\,Pa^a))$	τ_c (Pa)	a	χ^2_{obs}	$\dot{\varepsilon}_{CC}$(m/s)	$det(J^T J)$
1	204.7	3.24E-9	8.19	0.89	409.5	4.713E-8	6.25E-10
2	204.7	3.28E-9	8.26	0.88	409.5	4.714E-8	6.33E-10
3	204.8	3.53E-9	8.74	0.87	409.6	4.713E-8	5.64E-10
4	206.6	8.82E-10	0.00	1.19	413.2	4.713E-8	2.33E-04

Table 6
Solutions of artificial erosion profile for $m = 3$ and two experiments.

	f	k_d $(m/(s\,Pa^a))$	τ_c (Pa)	a	χ^2_{obs}	$\dot{\varepsilon}_{CC}(m/s)$	$det(J^T J)$
1	228.0	2.55E-9	6.72	0.95	456.1	4.722E-8	3.58E-10
2	228.2	3.06E-9	7.88	0.90	456.2	4.722E-8	3.42E-10
3	229.3	1.28E-9	2.37	1.10	458.5	4.722E-8	1.56E-09
4	230.6	8.75E-10	0.005	1.19	461.1	4.721E-8	1.14E-06

In both cases, the calculated interval for χ^2_{obs} was [378.6 494.2], and all solutions lie within it.

Table 7
Solutions with real experimental erosion profile.

	f	k_d $(m/(s\,Pa^a))$	τ_c (Pa)	$\dot{\varepsilon}_{CC}(m/s)$	$det(J^T J)$
1	3.159E-7	7.220E-9	29.58	1.771E-7	7.25E8
2	3.159E-7	7.224E-9	29.60	1.771E-7	5.90E3
3	3.159E-7	7.205E-9	29.50	1.773E-7	2.02E3
4	3.161E-7	7.304E-9	29.95	1.765E-7	3.77E9
5	3.166E-7	7.380E-9	30.24	1.762E-7	6.48E8
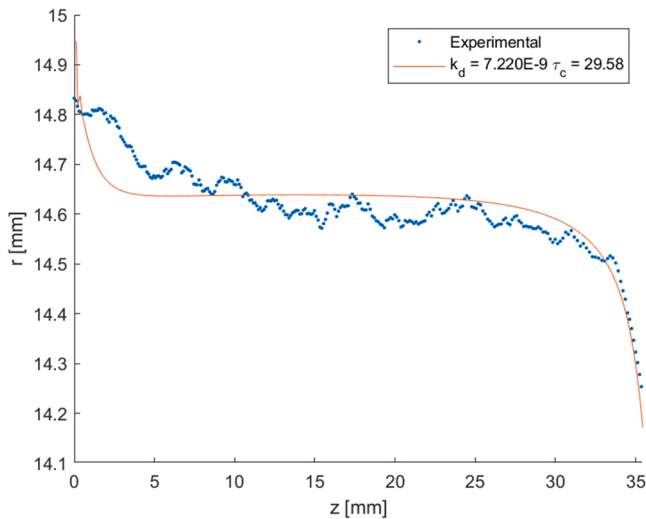
Fig. 8. Results of inverse calculation of parameters for real experimental erosion profile.

approximation does not necessarily lead to a good estimation of such intervals or regions; therefore, caution must be exercised. Other methods for calculating confidence regions, not based on linearisation, include the F-test, log-likelihood method, and Monte Carlo techniques. However, these methods require many more function evaluations, which translates to significant simulation effort. Linearisation was performed with the approximated Hessian matrix, which was computed using the Jacobian matrix calculated with difference approximations at the optimum solution ($H = J(\theta^*)^T J(\theta^*)$). The covariance matrix was approximated using Eq. (16), which was reported by Donaldson and Schnabel as the best linearisation approach [21] in terms of results and computation effort. The confidence intervals were calculated based on a t-student distribution with a confidence level of 95%, as shown in Eq. (17), with s calculated from Eq. (15):

$$Cov(\theta) = s^2 (J^T J)^{-1} \tag{16}$$

$$\theta \quad \pm \quad t_{\nu,0.975} \quad diag(Cov(\theta))^{\frac{1}{2}}. \tag{17}$$

Here, $diag(Cov(\theta))^{\frac{1}{2}}$ refers to a vector of m components obtained from the diagonal of the covariance matrix by taking the square root of each element.

The difference between the confidence intervals and regions is that the regions allow for correlations between the parameters. When using linearisation, the shape of the regions is elliptical, centred on the solution, as given by Eq. (18). The confidence level is determined from the χ^2 distribution with m degrees of freedom, as expressed in Eq. (19), for which a 95% confidence is employed.

$$(\theta - \theta^*)^T s^{-2} J^T J (\theta - \theta^*) \leq \Delta^2 \tag{18}$$

$$\Delta^2 = F^{-1}_{\chi^2,m}(0.95) \tag{19}$$

The Hessian and covariance matrices for the first solution presented in Table 7 are given as follows:

$$H = \begin{pmatrix} 9.153 \cdot 10^{11} & -123.403 \\ -123.403 & 7.927 \cdot 10^{-4} \end{pmatrix}; Cov$$

$$= \begin{pmatrix} 2.422 \cdot 10^{-21} & 3.771 \cdot 10^{-16} \\ 3.771 \cdot 10^{-16} & 2.797 \cdot 10^{-6} \end{pmatrix}.$$
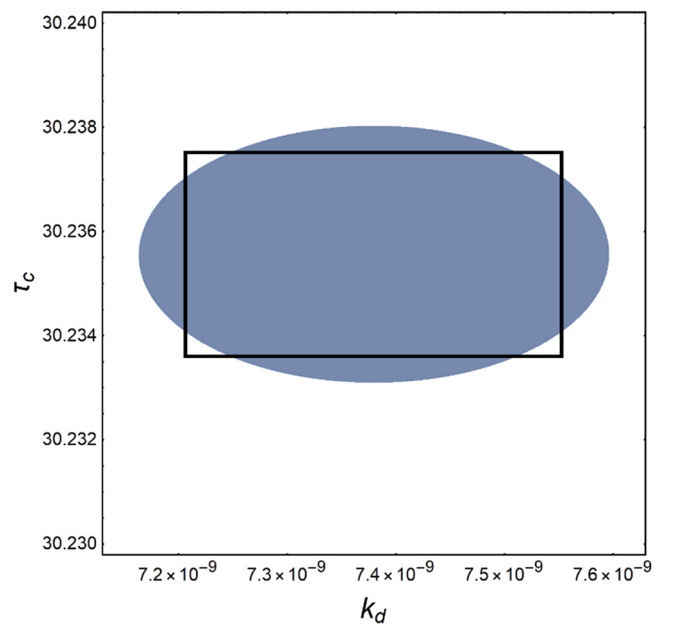
The confidence intervals are

$$7.123 \cdot 10^{-9} \quad \leq k_d \leq \quad 7.317 \cdot 10^{-9},$$

$$29.579 \quad \leq \tau_c \leq \quad 29.586.$$

The confidence intervals were narrow for both parameters. The confidence region is plotted in Fig. 9 with the box defined by the confidence intervals. It can be observed that both the region and intervals are similar, but the region is slightly larger.

The low inclination with respect to the parameter axis k_d can be observed from the coefficient of correlation between the parameters.

Fig. 9. Confidence regions (shaded ellipsoidal area) and confidence region (box) for solution 1.

Table 8
Confidence intervals and correlation coefficients for all solutions.

	$\bar{k}_{d_L}$	$\bar{k}_d$	$\bar{k}_{d_U}$	$\bar{\tau}_{c_L}$	$\bar{\tau}_c$	$\bar{\tau}_{c\,U}$	ρ_{k_d,τ_c}
1	7.12E-9	7.22E-9	7.32E-9	29.58	29.58	25.59	0.0046
2	7.01E-9	7.22E-9	7.43E-9	27.99	29.60	31.21	0.9433
3	6.66E-9	7.21E-9	7.75E-9	27.67	29.50	31.34	0.9817
4	7.24E-9	7.30E-9	7.37E-9	29.70	29.95	30.20	-1.0000
5	7.21E-9	7.38E-9	7.55E-9	30.23	30.24	30.24	0.0052

$$\rho_{k_d,\tau_c} = \frac{Cov(k_d,\tau_c)}{\sqrt{Var(k_d)Var(\tau_c)}} = 0.0046$$

Table 8 shows confidence intervals and parameter correlation for all solutions presented in Table 7, where the lower and upper bounds of the intervals are denoted with subscripts *L* and *U*, respectively. It can be observed that similar solutions, such as solutions 1 and 2, produce different confidence regions and parameter correlation. Therefore the reliability of the linearisation approach for the estimation of parameter confidence is not ensured and should be analysed for each individual case.

4. Conclusions

This study developed and tested a method for the inverse calculation of the erosion parameters of refractory materials in liquid slags. Investigations with a test problem proved that the problem is well suited for gradient-based solvers, and the NL2SOL solver can be employed. With the exact problem, identification of the true erosion parameters is achievable for both $m = 3$ and $m = 2$; however, the determinants of the Hessian matrix for $m = 3$ proves the difficulties associated with this approach.

An analysis with noisy generated erosion profiles revealed an ill-conditioning of the problem for $m = 3$. In these cases, multiple solutions were obtained and were equally acceptable; thus, erosion parameters could not be uniquely identified. This may be a result of the low variation in the WSS distribution along the axial coordinate. These results highlight the irrelevance of exact problems in the analysis of inverse-problem capabilities. The conclusions are confirmed by the determinant values of the Hessian matrices, which were close to singular for all cases with $m = 3$.

For the case of $m = 2$, where parameter *a* is set to 1, unambiguous identification was possible. However, local subminima were also encountered in the solution process, which suggest the necessity for using multiple random starting points. The results for the test problem were validated using the chi-square test.

Finally, the methodology was successfully applied to real experiments, in which the erosion parameters for a linear erosion rate could be identified. Confidence regions and intervals were also calculated; however, their reliability was not guaranteed because similar solutions produced dissimilar confidence regions. The methodology developed in this study is suitable for the inverse calculation of erosion parameters for refractory erosion in liquid slags and can guide further investigations of refractory erosion.

Even though the method has been mathematically extensively study, more experimental investigations are necessary to validate the erosion modelling approach chosen, specially the erosion law. This topic encompasses the current work of the authors and future investigations might concern the application of the method for different material/slag systems. An additional consideration comes from the fact that the erosion can be influenced by possible shear-thinning behaviour of the slag close to the refractory surface due to solid amounts; this would require a different modelling approach to the one described here. Specially a relationship between viscosity and solid content would be necessary as well as a characterization of the mass loss considering the granulometric composition. We believe that before considering such

effects it is justified and challenging to try to identify erosion parameters with the approach proposed here. Further, the evaluation with erosion profiles obtained from service conditions is of interest but it presents further challenges associated with the resolution of the flow-field for the given processes, where turbulence and other process-associated phenomena not included in this work may also be relevant.

CRediT authorship contribution statement

Jerónimo Guarco: Conceptualization, Methodology, Software, CFD Simulations and Optimisation software, Validation, Formal analysis, Investigation, Writing – original draft, Visualization. **Sandra Vollmann:** Conceptualization, Writing – review & editing, Supervision, Project administration. **Harald Harmuth:** Conceptualization, Writing – review & editing, Supervision, Resources, Funding acquisition. **Burhanuddin:** Investigation – Performing experiments.

Declaration of Competing Interest

The authors declare that they have no known competing financial interests or personal relationships that could have appeared to influence the work reported in this paper.

Data Availability

Data will be made available on request. The data that support the findings of this study are available on reasonable request from the corresponding author.

Appendix A. Supporting information

Supplementary data associated with this article can be found in the online version at doi:10.1016/j.mtcomm.2022.104736.

References

[1] S. Vollmann, H. Harmuth, CFD simulation of mass transfer coefficients relevant for refractory wear, Int. Ceram. Rev. Refract. (2012) 19–21.
[2] A.M. Guzmán, D.I. Martínez, R. González, Corrosion–erosion wear of refractory bricks in glass furnaces, Eng. Fail. Anal. 46 (2014) 188–195, https://doi.org/10.1016/j.engfailanal.2014.09.003.
[3] E. Partheniades, Erosion and deposition of cohesive soils, J. Hydraul. Div. 91 (1965) 105–139, https://doi.org/10.1061/JYCEAJ.0001165.
[4] A.-S.T. Al-Madhhachi, G.J. Hanson, G.A. Fox, A.K. Tyagi, R. Bulut, Measuring soil erodibility using a laboratory "mini" JET, Trans. ASABE 56 (2013) 901–910, https://doi.org/10.13031/trans.56.9742.
[5] G.J. Hanson, A. Simon, Erodibility of cohesive streambeds in the loess area of the midwestern USA, Hydrol. Process. 15 (2001) 23–38, https://doi.org/10.1002/hyp.149.
[6] Weidner K., Petrie J., Diplas P., Nam S., Gutierrez M., Ellenberg M. Numerical Simulation of Jet Test and Associated Soil Erosion, Paris: 2012.

[7] G.J. Hanson, K.R. Cook, Apparatus, test procedures, and analytical methods to measure soil erodibility in situ, Appl. Eng. Agric. 20 (2004) 455–462, https://doi.org/10.13031/2013.16492.

[8] T. Karmaker, R. Das, Estimation of riverbank soil erodibility parameters using genetic algorithm, Sādhanā 42 (2017) 1953–1963, https://doi.org/10.1007/s12046-017-0733-6.

[9] C.F. Wan, R. Fell, Laboratory tests on the rate of piping erosion of soils in embankment dams, Geotech. Test. J. 27 (2004) 295–303, https://doi.org/10.1520/gtj11903.

[10] J.L. Briaud, F.C.K. Ting, H.C. Chen, Y. Cao, S.W. Han, K.W. Kwak, Erosion function apparatus for scour rate predictions, J. Geotech. Geoenviron. Eng. 127 (2001) 105–113, https://doi.org/10.1061/(ASCE)1090-0241(2001)127:2(105).

[11] V. Kircher, Burhanuddin, H. Harmuth, Design, operation and evaluation of an improved refractory wear testing technique, Measurement 178 (2021), 109429, https://doi.org/10.1016/j.measurement.2021.109429.

[12] G.I. Taylor, Stability of a viscous liquid contained between two rotating cylinders. philosophical transactions of the royal society a: mathematical, Phys. Eng. Sci. 223 (1923) 289–343, https://doi.org/10.1098/rsta.1923.0008.

[13] R.C. DiPrima, P.M. Eagles, B.S. Ng, The effect of radius ratio on the stability of Couette flow and Taylor vortex flow, Phys. Fluids 27 (1984) 2403, https://doi.org/10.1063/1.864544.

[14] K.N. Astill, Studies of the developing flow between concentric cylinders with the inner cylinder rotating, J. Heat Transf. 86 (1964) 383–391, https://doi.org/10.1115/1.3688703.

[15] S. Chandrasekhar, Hydrodynamic and Hydromagnetic Stability, Dover Publications, Inc., New York, 1961, https://doi.org/10.1017/S0022112062210592.

[16] C.D. Andereck, S.S. Liu, H.L. Swinney, Flow regimes in a circular Couette system with independently rotating cylinders, J. Fluid Mech. 164 (1986) 155–183, https://doi.org/10.1017/S0022112086002513.

[17] J.E. Dennis, D.M. Gay, R.E. Walsh, An adaptive nonlinear least-squares algorithm, ACM Trans. Math. Softw. 7 (1981) 348–368, https://doi.org/10.1145/355958.355965.

[18] R.C. Aster, B. Borchers, C.H. Thurber, Parameter Estimation and Inverse Problems, Elsevier Inc,, 2013, https://doi.org/10.1016/C2009-0-61134-X.

[19] J. Guarco, H. Harmuth, S. Vollmann, Method for determination of mass transfer coefficients for dissolution of dense ceramics in liquid slags, Int. J. Heat Mass Transf. 186 (2022), 122494, https://doi.org/10.1016/j.ijheatmasstransfer.2021.122494.

[20] J. Xin, L. Gan, L. Jiao, C. Lai, Accurate density calculation for molten slags in SiO2-Al2O3-CaO-MgO systems, ISIJ Int. 57 (2017) 1340–1349, https://doi.org/10.2355/isijinternational.ISIJINT-2017-070.

[21] J.R. Donaldson, R.B. Schnabel, Computational experience with confidence regions and confidence intervals for nonlinear least squares, Technometrics 29 (1987) 67–82, https://doi.org/10.1080/00401706.1987.10488184.